metals

MDPI

Article

Two-Dimensional X-Ray Diffraction (2D-XRD) and Micro-Computed Tomography (Micro-CT) Characterization of Additively Manufactured 316L Stainless Steel

Puskar Pathak [1,2,3,*], Goran Majkic [1,2,3], Timmons Erickson [4], Tian Chen [1,2] and Venkat Selvamanickam [1,2,3]

[1] Advanced Manufacturing Institute, University of Houston, Houston, TX 77023, USA
[2] Department of Mechanical Engineering, University of Houston, Houston, TX 77204, USA
[3] Texas Center for Superconductivity, University of Houston, Houston, TX 77204, USA
[4] Jacobs-JETS, NASA Johnson Space Center, Houston, TX 77058, USA
* Correspondence: ppathak3@cougarnet.uh.edu

Abstract: In-depth quality assessment of 3D-printed parts is vital in determining their overall characteristics. This study focuses on the use of 2D X-Ray diffraction (2D-XRD) and X-Ray micro-computed tomography (micro-CT) techniques to evaluate the crystallography and internal defects of 316L SS parts fabricated by the powder-based direct energy deposition (DED) technique. The test samples were printed in a controlled argon environment with variable laser power and print speeds, using a customized deposition pattern to achieve a high-density print (>99%). Multiple features, including hardness, elastic modulus, porosity, crystallographic orientation, and grain morphology and size were evaluated as a function of print parameters. Micro-CT was used for in-depth internal defect analysis, revealing lack-of-fusion and gas-induced (keyhole) pores and no observable micro-cracks or inclusions in most of the printed body. Some porosity was found mostly concentrated in the initial layers of print and decreased along the build direction. 2D-XRD was used for phase analysis and grain size determination. The phase analysis revealed single phase γ-austenitic FCC phase without any detectable presence of the δ-ferrite phase. A close correlation was found between Electron Backscatter Diffraction (EBSD) and 2D-XRD results on the average size distribution and the crystallographic orientation of grains in the sample. This work demonstrates the fast and reliable as-printed crystallography analysis using 2D-XRD compared to the EBSD technique, with potential for in-line integration.

Keywords: additive manufacturing; LENS-DED; 316L SS; 2D-XRD; micro-CT

check for updates

Citation: Pathak, P.; Majkic, G.; Erickson, T.; Chen, T.; Selvamanickam, V. Two-Dimensional X-Ray Diffraction (2D-XRD) and Micro-Computed Tomography (Micro-CT) Characterization of Additively Manufactured 316L Stainless Steel. *Metals* **2024**, *14*, 1232. https://doi.org/10.3390/met14111232

Received: 12 September 2024
Revised: 17 October 2024
Accepted: 19 October 2024
Published: 29 October 2024

Copyright: © 2024 by the authors. Licensee MDPI, Basel, Switzerland. This article is an open access article distributed under the terms and conditions of the Creative Commons Attribution (CC BY) license (https://creativecommons.org/licenses/by/4.0/).

1. Introduction

The emergence of different additive manufacturing (AM) techniques for rapid prototyping evolved into high-value manufacturing in the aerospace, automotive, and medical sectors. The redesign of conventional parts to a new geometry enabled by AM provides benefits including lightweight, reduction in material waste and part cost, part consolidation, and enhanced performance. Among various metal AM techniques, direct energy deposition (DED) developed by Sandia National Laboratories under the name laser-engineered net shaping (LENS) utilizes thermal energy, typically laser/electron beam, to fuse powder/wire, which is fed directly to the melt pool forming structure layer by layer. DED is also referred to as laser melting deposition (LMD), direct melt deposition (DMD), direct laser deposition (DLD), and direct laser fabrication (DLF) [1]. Unlike the powder bed AM process, DED can be performed on uneven surfaces with a precision design finish, opening a range of complex repair applications and maintaining existing parts in the aerospace and automotive industries [2–4]. It has the unique capability of printing materials and integrating them with subtractive machining to finalize the surface finish and dimensions of the printed parts after 3D printing [5–9]. The resultant microstructure typically consists

of well-refined grains because of local rapid melting and cooling and can achieve 30% or higher strength compared with those built by casting [10,11].

Numerous research works have been conducted over the years on steel using the LENS-DED technique using different 3D print parameters to optimize their properties [1,5–7,12–16]. The 316L stainless steel (SS) is one of the most widely used low-carbon austenitic stainless steel in chemical industries, power generation, medical devices, and the marine sector. B. Zheng et al. studied the microstructure evolution of LENS-DED-printed 316L SS and its defect control and suggested the high thermal gradient and dynamic flow of the fast-moving melting pool to be responsible for controlling the microstructure and properties [15]. The effects of different process parameters and deposition strategies were studied on 316L SS using direct laser deposition [17–20]. Balhara et al. investigated the 316L using the LENS-DED technique and reported ripple formation, dendritic patterns, and a heterogeneous microstructure [21]. Various numerical studies of thermal behavior and microstructural evolution of the LENS-DED process were conducted to simulate the melt pool and cooling process during deposition [22–25]. The 316L SS alloy was also studied using powder bed fusion and material extrusion; different process maps were created to optimize deposition parameters to obtain high density and improved mechanical properties [9,26–30]. Mirzababaei et al. recently used the binder jet additive manufacturing of 316L to study microstructure–mechanical properties [31].

Real-time monitoring of thermal behavior during deposition and in situ inspection provides valuable information on build properties [32,33]. For example, monitoring a melt pool with an infrared camera (IR), high-speed camera, and acoustic sensors offers dimensional tolerance and surface property information [34]. For structure characterization, SEM, Micro-CT, and EBSD have been used [35–37] to characterize porosity, grain size distribution, and orientation distribution. However, techniques requiring a vacuum, for example, SEM/EBSD, are challenging to incorporate as potential in situ characterization tools. In addition, EBSD requires considerable sample preparation time and effort. Two-dimensional X-Ray diffraction (2D-XRD) is a very useful and versatile crystallographic characterization tool that can be readily adapted to metal AM to characterize the structure of 3D-printed metallic samples. Due to the use of an area (2D) detector to record diffraction patterns, it is a rapid and robust material characterization method that delivers essential information on the phases present, strain, grain size, and crystallographic orientation in a very short time [38,39]. Compared to a conventional diffractometer, 2D-XRD provides far more diffraction pattern information [39–41]. For porosity characterization, X-Ray micro-computed tomography (micro-CT) provides a non-destructive way to analyze internal features and map the distribution of the pores in 3D-printed parts [15,35,42]. It utilizes X-Ray as a source to record multiple images, which are reconstructed using a computer algorithm to form a 3D model, providing resolution down to sub-micrometer level [37,42]. It can also be used to measure geometrical accuracy by determining the zone of deviation (distortion) and comparing it with the original CAD part file [43,44].

In the current research, we conducted a systematic investigation involving the variation of laser power and the transverse speed of the 316L stainless steel using the directed energy deposition (DED)-based laser-engineered net shaping (LENS) technique. We produced samples by applying customized deposition patterns and subsequently assessed their density and micro-hardness. Our primary focus was on the comprehensive characterization of the printed components, which entailed thorough crystallographic analysis using 2D-XRD. We also correlated our findings by estimating grain size through the electron backscatter diffraction (EBSD) technique and conducted a detailed examination of micro-defects using high-resolution computer tomography (CT). The usage of the proposed characterization techniques is further discussed, and their results are presented with a potential for in-line integration.

2. Materials and Experimental Methods

2.1. Materials

Gas-atomized 316L stainless steel powder from Carpenter Additive (Philadelphia, PA, USA)was used to print the cube samples. We used scanning electron microscopy (SEM) for powder size and morphology analysis and micro-CT to analyze powder internal quality. The SEM image of the powder (Figure 1a) depicts the spherical atomized powder particles together with labels of locations where energy dispersive X-Ray spectroscopy (EDS) was performed, which shows a nominal number of major elements (Fe, Cr, Ni) present. The powder particle size distribution histogram (Figure 1b) reveals a range of 20 µm to 100 µm with an average size of 65 µm.

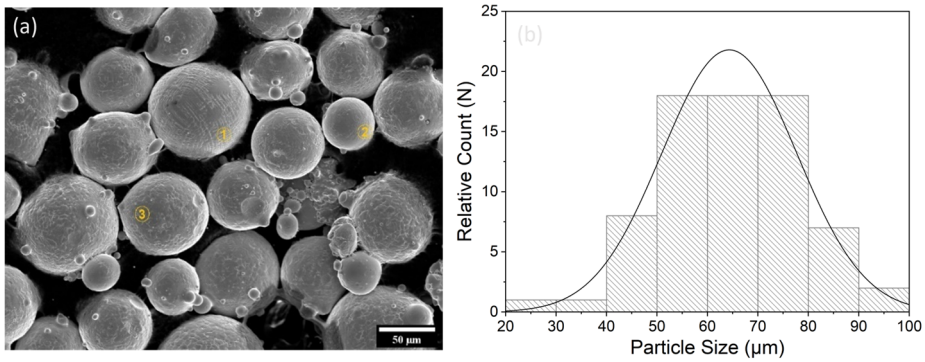


Figure 1. (**a**) SEM image of 316L SS powder with numbered locations of EDS analysis. (**b**) 316L SS particle size distribution.

2.2. Experimental Methods

The powder-based LENS-DED technique was used to fabricate test samples onto a 304 SS substrate. The LENS MTS 500 hybrid tool from Optomec Inc. (Albuquerque, NM, USA), used in this work enables deposition in a controlled Ar atmosphere for better control of microstructure evolution. An oxygen level < 10 ppm was achieved during the deposition by using argon as an inert gas. A Nd: YAG laser of wavelength 1068.7 nm, laser power of 1 kW, and 9.525 mm stand-off distance was used during the deposition process.

The parametric study in this work comprised increasing the laser power while keeping the powder feed rate and scanning speed constant (first set) and increasing the scanning speed with constant powder feed rate and laser power (second set). The first set of samples, i.e., S1 to S4, were printed with the parameters listed in Table 1, and the second set of samples, i.e., S5 to S8, with the parameters listed in Table 2 along with their respective specific energies. Specific energy (E), which is quantifying energy delivery per unit area of material, is a function of laser power (P), scanning speed (v), and laser beam radius (r_b), as presented in Equation (1). It is useful in predicting the occurrence of melting of any material under a particular set of parameters [45].

$$E = \frac{P}{2vr_b} \quad (1)$$

Table 1. Laser power parameters used for LENS-DED of samples S1–S4.

First Set (Powder Feed Rate: 7.89 g/min; Scanning Speed: 10 mm/s)		
Sample No.	**Laser Power (Watts)**	**Specific Energy (J/mm^2)**
S1	280	28.00
S2	340	34.00
S3	380	38.00
S4	420	42.00

Table 2. Scanning speed parameters used for LENS-DED of samples S5–S8.

Second Set (Powder Feed Rate: 7.89 g/min; Laser Power: 340 Watts)		
Sample No.	**Scanning Speed (mm/s)**	**Specific Energy (J/mm^2)**
S5	8	42.50
S6	10	34.00
S7	12	28.33
S8	16	21.25

In order to control the cooling rate and quality of the deposition, a custom deposition pattern was designed (Figure 2). The border of a layer is deposited first followed by filling the material inside the border using a bilateral pattern. Once a layer is fully deposited, a dwell time of 5 s is maintained for sample cooling, and the process is repeated for the next layer, but starting from another corner of the cube. The border printing and the change in scan direction with each subsequent layer as shown in Figure 2 is intended to control the geometric accuracy of the part. The change in the print location between the end of the previous and the start of the next layer is intended to increase the dwell time between layers at the same location for controlled cooling.

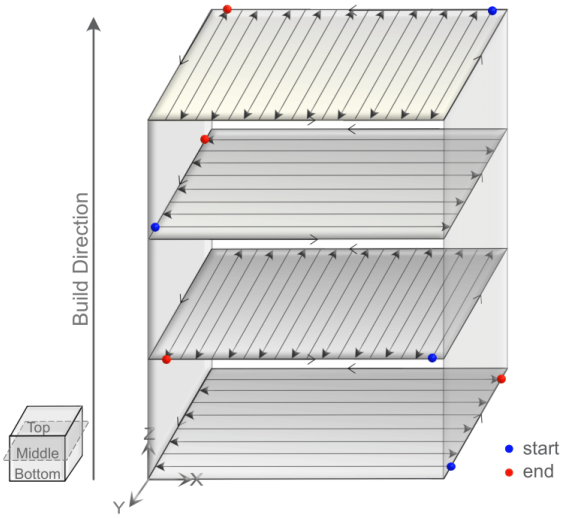


Figure 2. A schematic of the customized deposition pattern used in this study.

The as-printed samples were separated from the substrate and sectioned using an electric hacksaw. The sectioned samples were cleaned in an ultrasonic bath and mounted in epoxy resin along the build direction for metallographic sample preparation. Using Struers sample preparation steps [46], grinding and polishing were performed, followed by chemical etching using 15 mL HCl + 10 mL HNO_3 + 10 mL acetic acid for 30 s. Optical microscopy was used to view the sample's microstructure, cellular substructure, and boundaries. Scanning electron microscopy (SEM) and energy dispersive spectroscopy (EDS) with a 0.1 µm spot size were performed using Thermofisher Axia ChemiSEM (Waltham, MA, USA) for quantitative elemental composition and mapping. Grain orientation and mapping were conducted using the electron backscatter diffraction (EBSD) method. The samples were prepared by mechanical grinding, polishing, and final polishing with a vibratory polisher in 0.05 µm colloidal silica solution. The data were collected with a 0.5 µm step size using an Oxford Instruments Symmetry detector (Abingdon, UK) mounted on a JEOL 7900F (Tokyo, Japan) field emission scanning electron microscope with a 20 kV accelerating voltage and a 10 nA beam current. Archimedes' principle was used to measure the density of printed samples. The ZeGage Plus 3D (Middlefield, CT, USA) profilometer was used to measure the roughness of the samples by creating 3D roughness maps.

Two-dimensional X-Ray diffraction (2D-XRD) was performed using a Bruker D8 DISCOVER (Billerica, MA, USA) with a Vantec 500 General Area Diffraction Detector (GADDS) detector. The samples were scanned using a Cu K/α radiation (λ = 1.54 Å) source with an applied voltage of 50 kV and 1000 mA current. For all scans, a 0.5 mm beam size was used. The maximal depth of penetration of the XRD beam is ~7.5 µm at $2\theta = 90^\circ$ and the mass absorption coefficient (MAC) is 278.13 cm^2/g. For rocking curve scans, 12 sequential GADDS frames (detector positions) were collected with an exposure time of 240 s per frame. The 12 frames were stitched using a MATLAB code and analyzed to identify corresponding crystallographic peaks. In addition, {111} pole figure scans with detector centered at {111} and sample rotation about the surface normal (φ-scan) were conducted over 360° in 1° increments and 10 s exposures. Each sample was scanned at 2 different positions (i.e., top and bottom of the build direction) to study the variation in crystallographic orientation along the build direction. Moreover, the lattice constant and micro-strain of the scanned samples were calculated using the Nelson–Riley and Williamson–Hall extrapolation methods, respectively.

The internal print quality of the 3D-printed specimens was inspected using the Zeiss Xradia 520 Versa system (Oberkochen, Germany). The imaging was conducted at 140 kV with a 0.5 Cu filter at a resolution of 4 µm per pixel. The layer-wise porosity was calculated to visualize the internal defects by generating the 3D model of scanned samples and masking the bulk metallic and air volume to get the volume fraction of pores.

Micro-indentation was performed on the epoxy-mounted finish samples using Micro Combi Tester: MCT^3 indentation. A maximum loading force of 5N was applied with a loading/unloading rate of 1000 mN/min and a dwell time of 10 s. An average of five indentations were performed on the top, middle, and bottom sections of samples along the build direction to confirm the reproducibility of measured results. The respective reduced elastic modulus (E*) was calculated using the Oliver Phaar method [47–49].

3. Results

3.1. Surface Roughness and Density

The surface roughness (S_a) of as-printed samples was analyzed with a 3D profilometer (Supplementary Materials), which showed varying S_a values with changing laser power and scan speeds. An average S_a value of 14.1 µm was recorded. For both increasing laser power and scanning speed parameters, a tendency to a minimum in roughness was observed around 34 J/mm^2. From Archimedes density measurements [50] an average relative density of 99.02% of as-printed samples was achieved. All samples had a relative density of over 98%, ranging from 98.3 to 99.6%. The variation in the relative density of the samples was random and not correlated with different specific energy, laser power, or scanning speed associated with the printed samples.

3.2. Microstructure

Figure 3a,b show SEM micrographs of the S8 sample along the build direction. It reveals a cellular substructure with a small fraction of induced pores. The microstructure evolution shows multiple cellular colonies consisting of both columnar and equiaxed cellular domains with a small fraction of pores due to different thermal histories and solidification rate conditions experienced during deposition. The presence of equiaxed and columnar sub-structures is also visible within the microstructure; a similar result was shown by Yadollahi et al. [17]. The same features have been reported by Balhara et al. [21], who report heterogeneous columnar/equiaxed cellular substructure formation along the build direction. Pacheco et. al. attributed the formation of the cellular structures to the rapid solidification of the melt pool after each subsequent layer of deposition [18]. It should be noted that the cellular domains/substructures do not coincide with grains. At the bottom section of deposition, the printed layers experience a rapid quenching effect of a high cooling rate of 10^3 to 10^4 K/s [22]. However, as the print layers increase, the repeated laser melting and solidification hinder the cooling rate, resulting in a coarser

microstructure. A similar result was observed by Yadollahi et al. [17]. Figure 3b shows the locations of EDS for elemental distribution analysis. The EDS analysis was performed on six different points; spots 1 and 3 on cellular substructure (G), spots 2 and 4 on domain boundaries (B), and spots 5 and 6 on pores (P). The EDS results for S8 are presented in Table 3. Within each of the features (G, B, P), the composition is consistent. However, compared to the cellular substructure, domain boundaries show a pronounced decrease in Fe content and a corresponding increase in Cr, Mo, and Si levels. The pores exhibit a similar composition relative to cellular domains, which is expected for the pores located inside the cellular substructure.

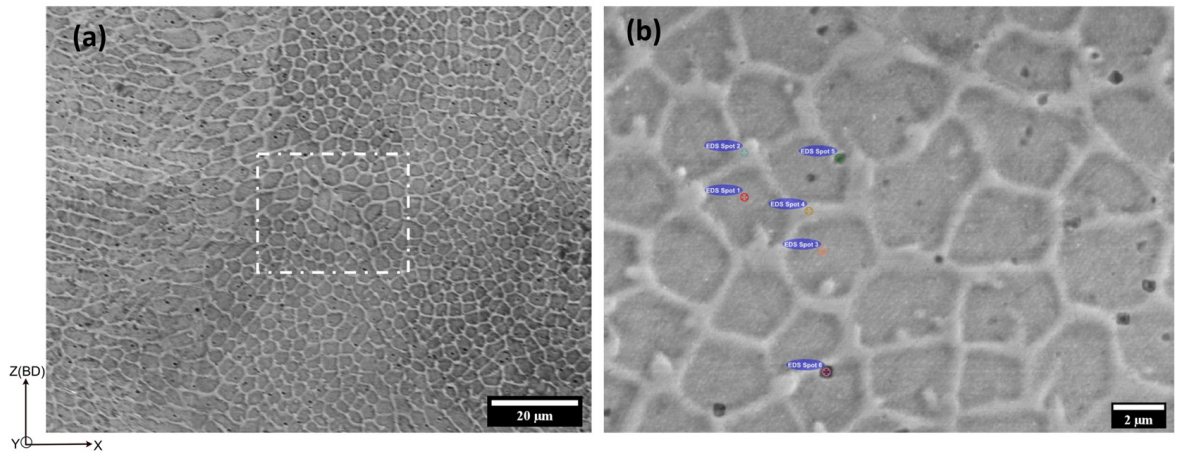


Figure 3. (**a**) SEM micrograph of the S8 printed sample; (**b**) micrograph of the center area in (**a**) at higher magnification with locations of EDS analysis.

Table 3. EDS point analysis of the S8 sample.

	Elements (wt.%)					
Spot No.	**Fe**	**Cr**	**Ni**	**Mo**	**Si**	**Mn**
G1 (spot 1)	66.9	18.8	12.0	1.3	0.3	0.7
G2 (spot 3)	67.1	18.6	11.9	1.3	0.3	0.7
B1 (spot 2)	61.7	21.4	12.1	3.2	0.6	0.7
B2 (spot 4)	61.9	21.1	13.1	2.5	0.8	0.7
P1 (spot 5)	65.7	19.6	11.8	1.3	0.8	1.4
P2 (spot 6)	65.7	20.2	10.9	1.7	0.3	1.3

The grain orientation and morphology were analyzed using the EBSD technique for samples S2, S4, and S8. Figure 4 shows the EBSD map and pole figure of S2, S4, and S8 samples along the build direction. The grains with the same crystallographic orientation are represented by the same color, and each color represents a different combination of Euler's angles. The grain maps in Figure 4a,c,e show a heterogeneous grain structure with irregular morphology. Most grain boundaries in the S2 sample exhibit a large misorientation > 10°, i.e., 19.1% of boundaries are aligned within 2 to 10° and 80.9% show a misorientation > 10°. In the S4 sample, 13% of boundaries are aligned within 2 to 10° and 87% are misoriented > 10°. In the S8 sample, 33.7% of boundaries are within 2 to 10° and 66.3% are oriented > 10° (Supplementary Materials). The dark-colored region in Figure 4c is identified as local porosity within the microstructure. We note that the number of grains sampled is relatively low to conclude that the print parameters for S8 lead to a larger number of small misorientation boundaries. The dark-colored regions were identified as local porosity within the microstructure. The phase map indexing analysis showed the presence of only a single γ-FCC austenitic phase. The unstable BCC ferrite phase [51]

was not detected in any of the samples, whereas some studies in the literature reported the presence of a small fraction of δ-ferrite in their studies [15,17,26,31,36]. Yadollahi et al. demonstrated a decreased volume fraction of the ferrite phase by employing the heat treatment method and achieving full austenitic grains [17]. The average grain size was measured from EBSD by taking the square root of the area occupied by grains divided by the number of grains, resulting in approximately 160, 115, and 93 µm for S2, S4, and S8, respectively. We note that the scanned area is small relative to grain size to accurately determine the average grain size from these EBSD images; however, the values still provide insight into the grain size. The corresponding pole figure contour diagrams in Figure 4b,d,f depict a random orientation of grains with a strong intensity along (100).

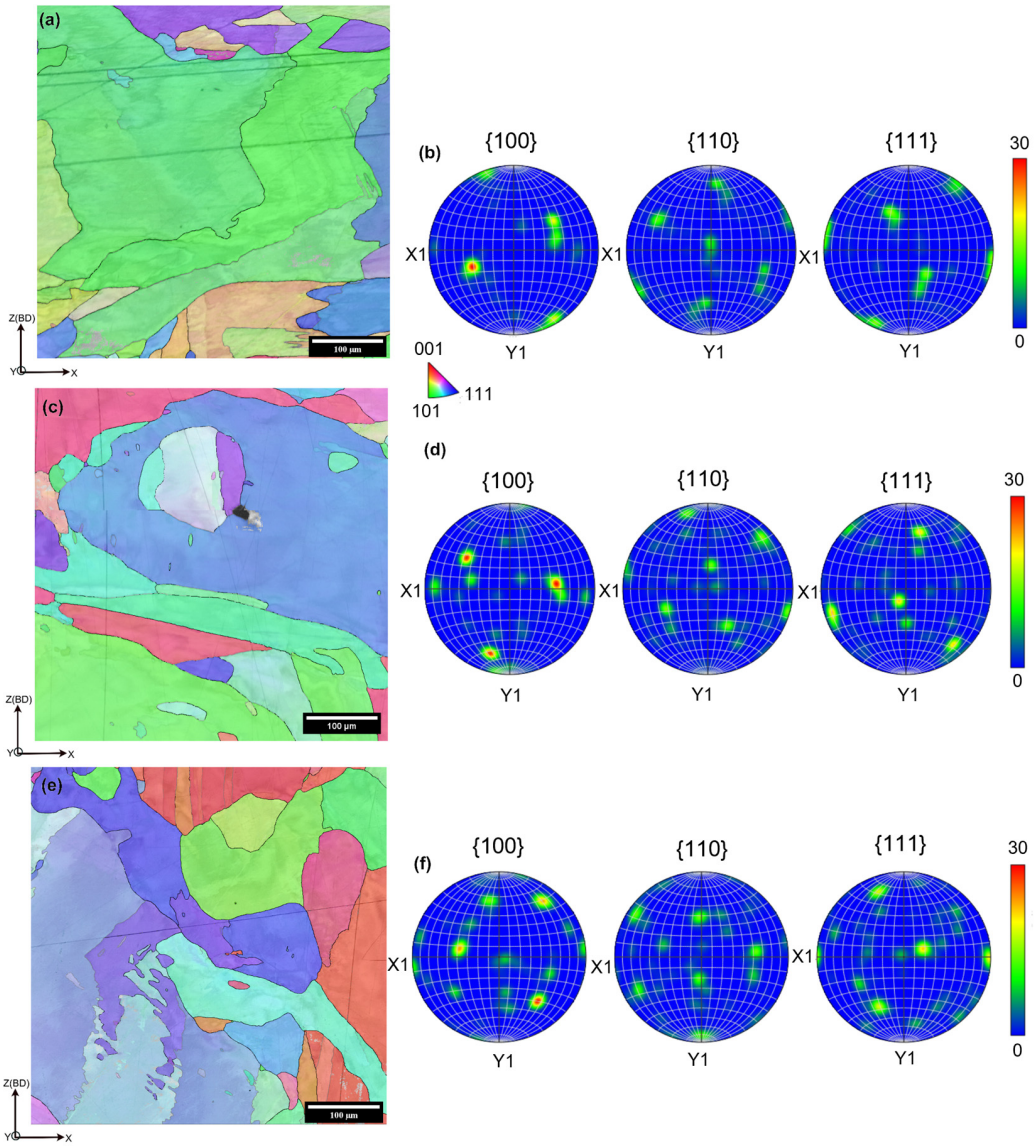


Figure 4. EBSD orientation maps of S2 sample (**a**), S4 sample (**c**), and S8 sample (**e**) along the build direction and (**b**,**d**,**f**) corresponding to {100}, {110}, and {111} FCC-iron pole figures, respectively.

3.3. 2D XRD Analysis

Figure 5 illustrates the rocking curve 12-frame stitched 2D-XRD patterns of samples scanned at two different locations (i.e., top and bottom sections) along the build direction. The x and y axes are the χ and 2θ angles, respectively, where χ is the angle relative to the sample's normal direction. The 316L SS phase is randomly distributed, as indicated by the random distribution of χ angles of diffraction peaks along the identified peak at 2θ

locations. It also reveals the presence of a single austenitic FCC phase with no foreign phase peaks detected. The crystallographic planes {111}, {200}, {220}, and {311} were identified at 2θ angles of 43.61°, 50.68°, 74.57°, and 90.50°, respectively (Figure 5). Although a fully austenitic γ phase was present in all samples, the crystallographic peaks show different full-width-at-half-maximum (FWHM) values. An average lattice constant and micro-strain of 3.59 ± 0.001 Å and 2.49 × 10^{-3}, respectively, were calculated for powder 316L SS. The corresponding values were 3.59 ± 0.003 Å and 3.62 × 10^{-3} for S2, 3.59 ± 0.029 Å and 3.04 × 10^{-3} for S4, and 3.60 ± 0.002 Å and 2.86 × 10^{-3} for S8 printed samples. The lattice constant is apparently unaffected by the print parameters; however, the micro-strain appears to be consistently larger in printed samples compared to the starting powder.

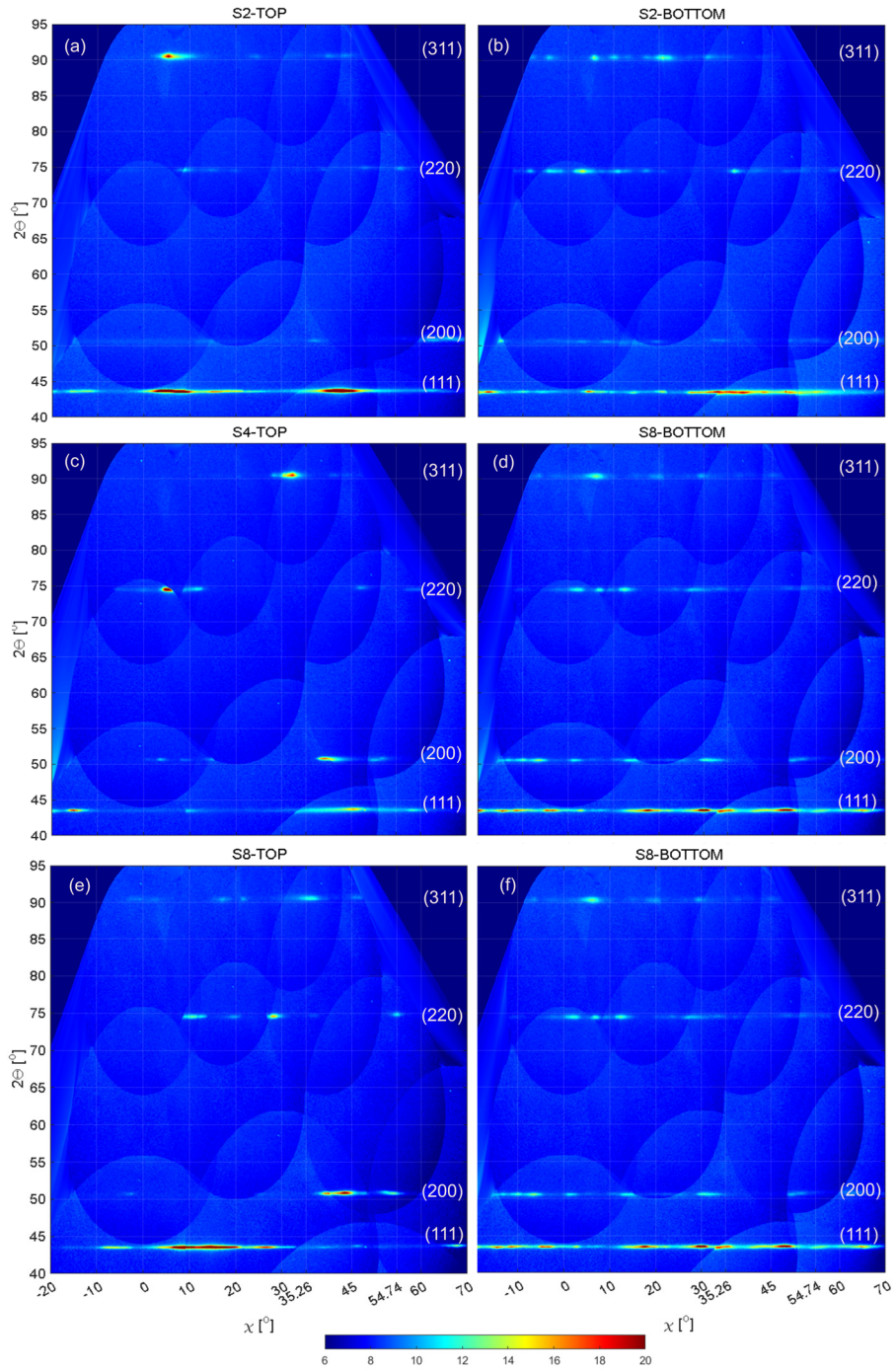


Figure 5. Rocking curve 12-frame stitched 2D-XRD patterns of 2θ vs. χ (**a**,**b**) S2 top and bottom sections; (**c**,**d**) S4 top and bottom sections; (**e**,**f**) S8 top and bottom sections, respectively.

Pole figure scan using 2D-XRD provides in-detail crystallographic orientation maps [38]. The 316L metallic sample {111} peak at 43.61° 2θ angle was analyzed at two different sections along the build direction. As shown in Figure 6a,b, the {111} peak texture of the S2 sample top section reveals a larger grain size manifested by a lower peak count and stronger intensity compared to the S2 bottom section where smaller grain size with higher grain count and lower intensities are observed. A similar feature is observed in Figure 6c–f for S4 and S8 samples, respectively. Further, the top sections of samples S4 and S8 in Figure 6 reveal several intense peaks indicative of large grain sizes.

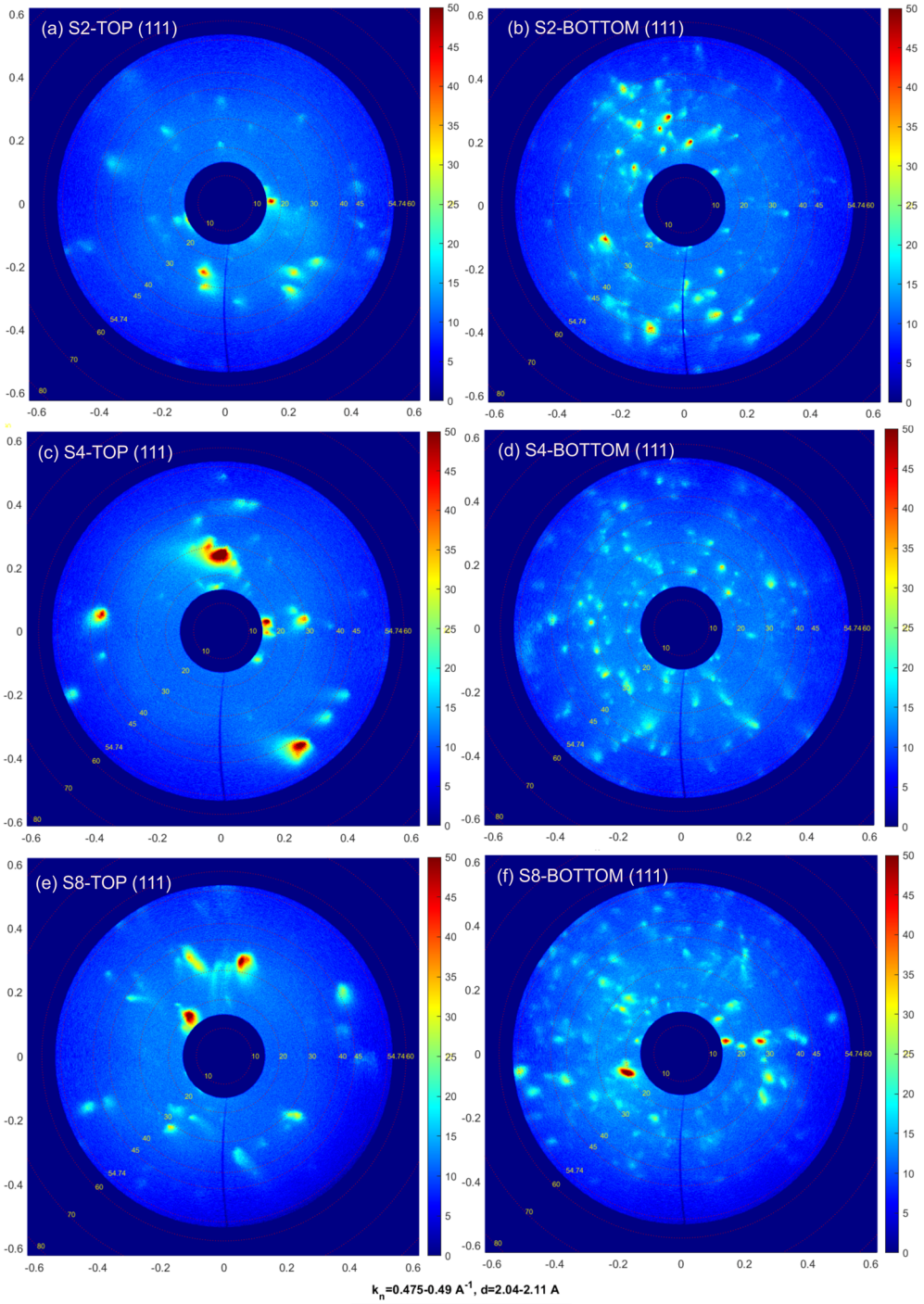


Figure 6. Pole figure of {111} peak. (**a**,**b**) S2 top and bottom sections; (**c**,**d**) S4 top and bottom sections; (**e**,**f**) S8 top and bottom sections, respectively.

The peak count and peak intensity distribution could, in principle, be used to extract grain size and distribution information. Several attempts have been reported in the literature [39–41,52]. As a first approximation, using the pole figure, an estimate of grain size (D) can be estimated based on the number of observed {111} peaks and using Equation (2).

$$D = \sqrt{\frac{A_{pf}}{N_{grains}}} \quad (2)$$

Here, A_{pf} is the X-Ray illuminated area of the sample and N_{grains} is the total grain count, determined from the number of observed {111} peaks normalized by the multiplicity and fraction of reciprocal space scanned. It should be noted, however, that there are complexities arising from scan geometry. For instance, the projection of the incident circular X-Ray beam of diameter d on the sample is an ellipse with axes $a = d/sin\theta$ and $b = d$. During the rotation of the sample in the pole figure scan, only the area within a circle of diameter d inscribed inside the ellipse is illuminated for all 360° rotations. The rest of the ellipse area illuminates other grains for only a fraction of the 360° scan. This brings about two effects on the scan: (1) the intensity of the peaks originating from the area outside the inscribed circle will be lower than those inside it, and (2) the grains outside the circle will have a lower multiplicity of peaks. The first effect increases the uncertainty in using peak intensity as a measure of grain size, and the second effect affects the peak count as a measure of the number of grains. At a higher 2θ angle, the effect is less pronounced. Several strategies can be employed to minimize or eliminate this effect, e.g., sample oscillation in x/y directions to achieve continuous or near-continuous illumination of the same area during the scan. Another approach is to utilize calculated statistics and probabilities of observing reflections in the area outside of the inscribed circle. This is an ongoing effort that will be published separately.

Rocking curve measurements are in principle much faster, at a cost of partial loss of spatial distribution information (only χ angle distribution is obtained). However, this approach can also be utilized to estimate grain size, with similar considerations, including varying illumination angles and the statistical probability of grains being at diffraction conditions. It does readily provide qualitative insight into differences in grain size, similar to pole figure measurements, as shown in Figure 6. Approximations of grain size can be done for both using simplified assumptions. For the pole figure, using a simplifying assumption that most of the reflections come only from the inscribed circle, grain size can be estimated using $A_{pf} = d^2\pi/4$ in Equation (2). Furthermore, a full multiplicity of reflections can be assumed, e.g., M = 8 for {111} peaks, and the count can be normalized for the fraction of the reciprocal space {111} sphere scanned. In the case of the scans in Figure 6, χ ≈ 15–56° and the scanned area fraction relative to the full sphere is ≈20%. Based on this approach and peak counts from Figure 6, we estimate the grain size as shown in Table 4. For each pole figure, there is some uncertainty in peak count coming from the faintest peaks that could be interpreted as either noise or actual peaks. The grain size range in Table 4 reflects this uncertainty.

Table 4. Grain size estimation from the pole figures.

	Grain Size, D (μm)						
Samples	**Top**		**Bottom**		**Average**		**D(Top)/D(Bottom)**
	Max	Min	Max	Min	Top	Bottom	
S2	112	104	62	57	108	59	1.8
S4	110	104	54	51	107	53	2.0
S8	106	101	54	52	103	53	1.9

In a rocking curve, a smaller fraction (≈5%) of reciprocal space {111} is sampled. Moreover, only the grains that are oriented favorably for diffraction will contribute to the peak count. While these considerations are considered by multiplicity, for large grains and therefore small statistical count, multiplicity expectations will not be fully satisfied and a smaller peak count than expected will be encountered. Shown in Table 5 is the peak count and estimated grain size based on 12-frame rocking curve measurements. The grain size is overestimated due to small sampling statistics, as expected. This is particularly noticeable for the top section with a larger grain size and thus a very small count of only 7–8 peaks. For this reason, the ratio of the grain size estimate for the bottom and top sections is also lower compared to the pole figure estimate (1.5 vs. 2). However, the rocking curve method still reveals the differences between the top and bottom and provides an estimate for grain size.

Table 5. Grain size estimation from the rocking curves.

	Peak Count		Grain Size (μm)		
Samples	**Top**	**Bottom**	**Top**	**Bottom**	**Ratio (Top/Bottom)**
S2	7	13	161	118	1.4
S4	7	16	161	106	1.5
S8	8	15	150	110	1.4

The method for determining grain size from 2D-XRD can be improved. The illuminated area can be readily increased by a factor of four by doubling the beam size (1 mm collimator) with no increase in scanning time. For EBSD, to achieve the same sampling area increase, the scanned area would need to be increased four-fold, resulting in a 4× increase in scan time. Oscillation of samples along in-plane (x-y) directions while scanning can be readily introduced to increase scan area and thus peak count. In addition, a different scan approach can be used. For example, instead of a rocking curve, a φ scan could be conducted, similar to a pole figure, but with all peaks collected/integrated into a single frame. A potential problem with such an approach is that two or more peaks at the same χ location may overlap, resulting in misinterpretation of multiple smaller peaks as one intense peak. The probability of the overlap increases with an increase in the φ range scanned and a decrease in grain size. However, the φ scan can then be readily tailored for angular coverage of less than 360° to an optimum between the number of peaks collected and the probability of overlap.

We conclude that both pole figure and rocking curve can be used to estimate the grain size of 3D-printed metal parts. While rocking curve scans as conducted in this study overestimate grain size, they are significantly faster and still provide insight into grain size variations between bottom and top sections. Pole figure measurements required 720 frames in comparison with the rocking curve's 12 frame scans. Even though the scan time per frame was selected to be much longer for rocking curve measurements compared to pole figure (720 vs. 10 s) for the data shown in Figures 5 and 6, rocking curves collected for 30 s per frame also captured all but the smallest grain peaks that may be masked by noise. Furthermore, while 12 frame scans were used, we note that for grain size determination alone, all of the {111} information is captured by only three frames. Therefore, a potential 80-fold increase in scan speed can be achieved using rocking curves instead of pole figures at the expense of accuracy. Compared to EBSD, the 2D-XRD technique requires no vacuum and has the potential to be integrated as an in situ monitoring tool.

3.4. X-Ray Micro-CT

Reconstructed 3D-rendered images of all S2, S4, and S8 samples are shown in Figure 7, where the distribution of porosity along the build direction was reconstructed. The distribution of pores is mainly concentrated at the initial layers of the print. The region of interest (ROI) scan of the S8 sample in the bottom section reveals the presence of mainly two types of pores, gas-induced pores and lack-of-fusion pores, as can be distinguished by their shape and location [37,43]. Interconnected pores were also noticed, which might be due to the combination of keyhole pores and lack-of-fusion pores. No signs of micro-cracks or inclusions (foreign elements) were detected in all printed samples. Shown in Figure 8 is integrated porosity vs. build height, obtained from original 3D scans by cross-sectional integration. At the initial print layers, a higher porosity was observed at the bottom section; however, above the initial print layers, average porosity drops. It can also be noted, both from Figures 7 and 8, that the initial porosity seems to be layered, i.e., three porous layers separated by dense material, as can be seen for S2, S4, and S8 in particular. The origin of this layered structure could be due to the initial unstable powder flow through the nozzle and the colder substrate temperature. As shown in Tables 1 and 2, samples S4 and S8 are associated with higher laser power and scanning speeds, with 42 J/mm^2 and 21.25 J/mm^2 specific energy, respectively, compared to sample S2 with 34 J/mm^2. This increase in laser power and scanning speed had a deteriorating effect on the increase in pore fraction.

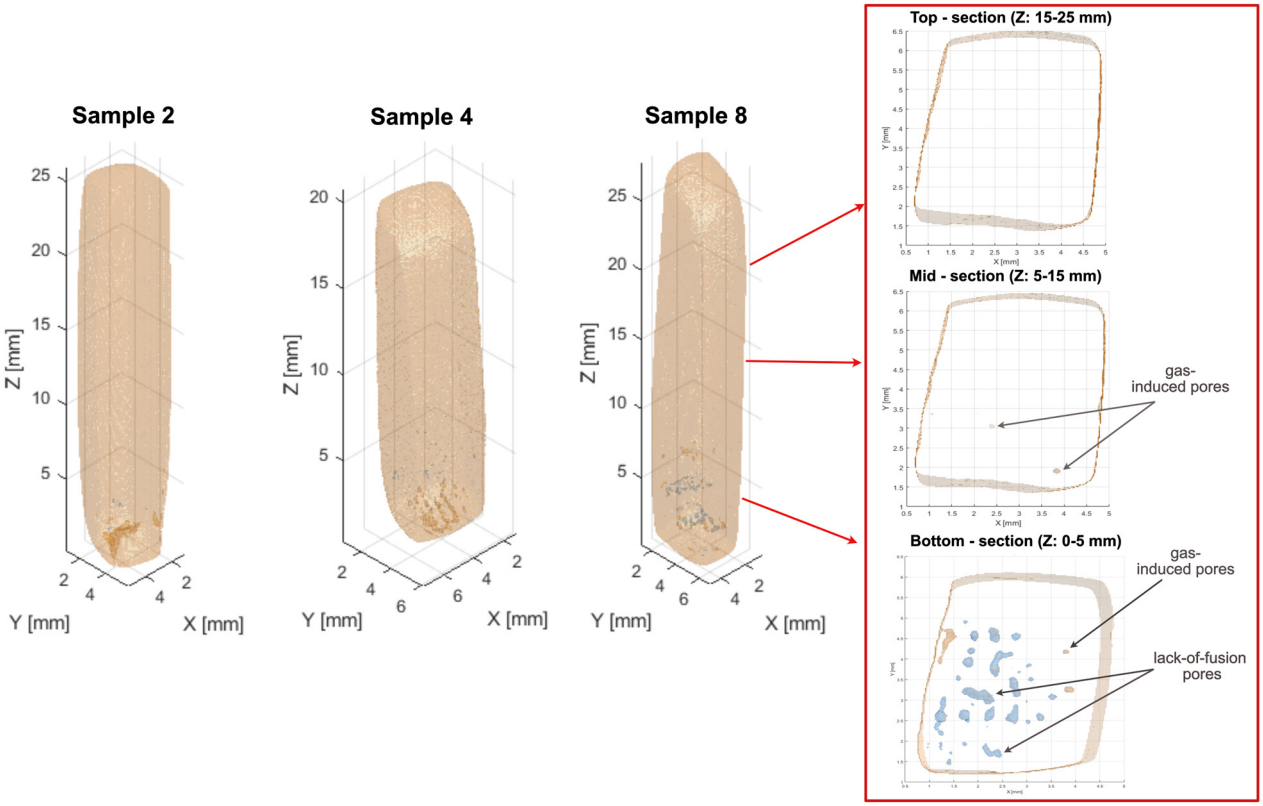


Figure 7. (**Left**) X-Ray micro-CT-reconstructed 3D images showing the distribution of the pores along the build height of all S2, S4, and S8 samples. (**Right**) a magnified higher resolution region of interest (ROI) scan at the top, middle, and bottom sections of the S8 sample, revealing the morphology and distribution of porosity.

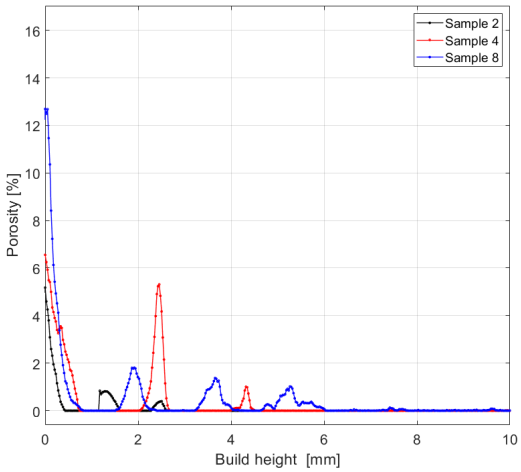


Figure 8. Porosity variations in S2, S4, and S8 samples along the build height.

3.5. Micro-Hardness Test

The microhardness of the samples was measured along the build direction, and an average of five indentations was conducted on every three sections of the samples. Along the build direction, different thermal histories were experienced by print layers, and the micro-hardness (HV) values were not uniform. Figure 9a depicts the variation in HV along the layer thickness, and the inset shows an indentation mark without any edge crack. The bottom section near the substrate experiences a higher cooling rate. This results in a smaller grain size and higher HV in the bottom section for all samples, consistent with the smaller grain size observed. For S2, HV values vary as 221.67 ± 1.12, 218.6 ± 0.88, and 209.87 ± 2.05 for the bottom, middle, and top sections, respectively. The corresponding values for the bottom, middle, and top sections of S8 are 266.67 ± 1.34, 228.23 ± 2.12, and 225.16 ± 0.88, respectively. Figure 9b presents the average indentation hardness (HV) and indentation elastic modulus (E*) of all samples. The average E* values for S2, S4, and S8 samples are 200.87 ± 1.12 GPa, 161.72 ± 1.73 GPa, and 191.24 ± 1.28 GPa, respectively. Although there is a considerable scatter in data, the Vickers scale HV and E* value show a decreasing trend with an increase in laser power and an increase with increasing scanning speed, as shown in Figure 9b.

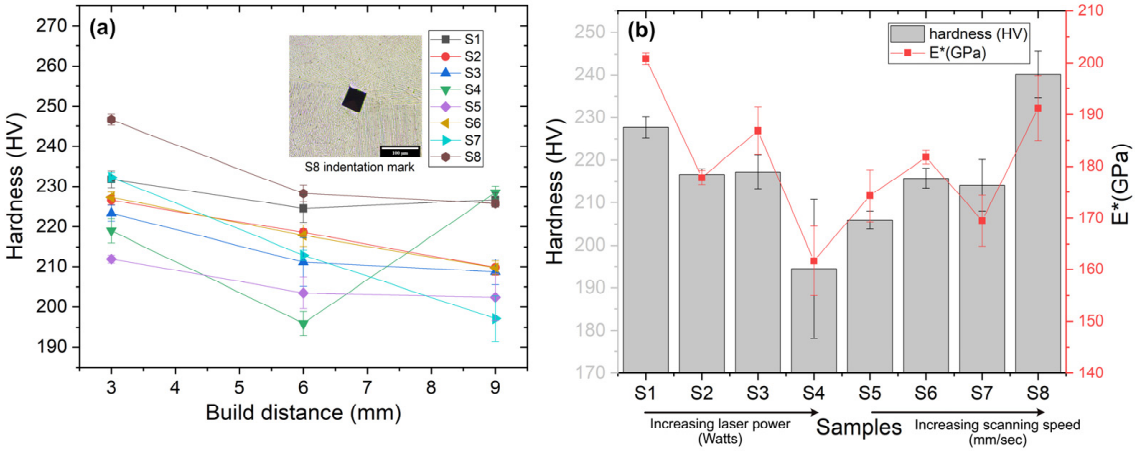


Figure 9. (**a**) Micro-hardness variation along the build distance of samples. (**b**) Samples' average indentation hardness (HV) and indentation elastic modulus (E*) plot.

4. Discussion

4.1. Microstructure Analysis Using 2D-XRD and EBSD

The present work demonstrates the usability of 2D-XRD for the characterization of the microstructure of parts made using additive manufacturing. Various types of scans are available, and they can be tailored to the specific goal, ranging from Williamson–Hall strain determination, detection and identification of secondary phases, and their relative amounts to grain size determination. It also has the potential to obtain grain size distribution via peak intensity distribution, as discussed earlier in the text. Grain size determination has been demonstrated in this study, with noted limitations and potential routes for improvement of the scanning method itself as well as data analysis. It is also non-destructive and can provide a similar level of information compared to EBSD without the need for sample polishing. It can be potentially integrated as an inline monitoring tool. With the 2D-XRD system installed inside the DED system, in situ crystallographic information of samples can be extracted; this offers quality inspection of the fabricated parts.

Grain size determination from pole figure measurements (Figure 6) has yielded comparable results to EBSD analysis (Table 4). We do reiterate that the simplified analysis used in this study is likely to bias the grain size to some extent as only the grains inside the inscribed circle of the illuminated area are scanned fully over the 360° range. We identify potential routes for further improvement, including an increase in collimator size and sample oscillation during scanning to increase sampled area and reduce the fraction of partially illuminated grains. We also note that the pole figure analysis can be further improved by determining the exact multiplicity of individual grains. As individual poles arising from the same grains have fixed angular relationships as well as comparable intensities (theoretically identical, practically varying only due to X-Ray geometry), multiple peaks from the same grain can be identified and consequently, the accuracy of the multiplicity factor can be improved over the constant multiplicity assumption, resulting in improved grain size determination accuracy. This task can be readily automated with coding.

Grain size from rocking curve measurements (Figure 5) has shown its potential to reveal differences in grain size from region to region. However, due to the limited peak count originating from a small subsection of reciprocal space, it tends to overestimate grain size (Table 5). The advantage, however, is in reduced scan time. We identify routes for improvement in the accuracy of the technique, which is similar to those suggested for improvement of pole figure measurements, with the addition of the possible use of a phi scan in order to increase the number of sampled grains.

4.2. Internal Defect Analysis Using Micro-CT

Micro-CT is particularly suitable for non-destructive evaluation of internal defects. The technique has limitations such as limited applicability to large objects, difficult implementation for on-site inspection, and relatively long scans, where other techniques may be more suitable. However, for research and development purposes ranging from optimization of the DED process itself to material-specific optimization on samples like those used in this study, it has been demonstrated to be particularly suitable and valuable in revealing internal defects to a great level of detail.

During the deposition process, as the initial powder metal pool of the print layer strikes the substrate, the mismatch in temperature gradient between the print layer and substrate causes some metal powder to scatter and leave un-melted particles in print [53]. This creates a higher distribution of lack-of-fusion pores at the bottom section, and as print layers increase, the accumulation of heat decreases the temperature gradient, which contributes to the improvement in print quality (Figure 8). Gas-induced pores, which are typical of small spherical shapes, are formed due to the presence of trapped gas in metal powder during vapor recoil keyhole laser melting [53,54]. On the other hand, the lack-of-fusion pores are irregularly shaped, seen mostly near layer boundaries, and formed by insufficient laser energy or non-optimized print parameters, which causes partial or unmolten powder melt pools [55,56]. As depicted in Figure 7, the presence of micro-cracks due to hot cracking

and inclusion defects due to foreign elements was not detected in all the samples. It was observed that by increasing the laser's specific energy, the lack-of-fusion pore fraction decreases to some extent; however, at a higher specific energy, keyhole formation was prominent (Figure 8), similar to the results reported in [13,57]. The presence of these pores was found to deteriorate the mechanical property and service life of printed parts [44,58]. The proper selection of process parameters, feedstock powder selection, and heat treatment process [44,59,60] were some reported techniques for controlling internal defects.

5. Conclusions

This article reports on the detailed assessment of 316L SS parts produced using a customized deposition pattern LENS-DED process in an Ar environment with varying laser power and scanning speeds. An in-depth analysis of microstructure evolution, texture, internal defects, and hardness was carried out to assess the printed parts. The samples showed a cellular heterogeneous microstructure with the presence of both columnar and equiaxed substructures with minor inter-grain chemical segregation. A variation in HV hardness along the print layers was observed for different samples due to their different specific energy (E) used for printing, resulting in different grain sizes. A detailed defects analysis using micro-CT revealed the presence of gas-fused (keyhole) pores and a lack-of-fusion pores without any micro-cracks and inclusions. A substantial pore fraction was found mostly concentrated at the initial layer of prints and decreases along the build direction.

An emphasis was placed on the evaluation of the use of 2D-XRD for microstructure analysis of parts made by additive manufacturing. For detection of secondary phases, the 2D-XRD method revealed a single austenitic γ-FCC phase without any trace of secondary δ-ferrite phase or other crystalline inclusions. Both pole figure and rocking curve measurements demonstrated that 2D-XRD can readily detect variations in grain size. Grain size in the bottom of the build direction was found to be approximately half of the grain size in the middle and top sections ($\approx$50 vs. 100 μm), which was attributed to lower average temperature at the beginning of the build. Grain size estimation from pole figure measurement was in close agreement with EBSD. Rocking curve measurements overestimated grain size due to lower peak count statistics. Sources of error for both approaches and routes for their minimization or elimination have been identified.

Supplementary Materials: The following supporting information can be downloaded at: https://www.mdpi.com/article/10.3390/met14111232/s1, Figure S1: 3D roughness map of S8 sample; Figure S2: Optical micrographs of (a,b) S2 sample; (c,d) S8 printed samples showing the presence of both cellular columnar and equiaxed substructure. The area bounded by dashed lines in (a,c) are magnified in (b,d) respect; Figure S3: EBSD map for S2 sample; Figure S4: EBSD map for S4 sample; Figure S5: EBSD map for S8 sample.

Author Contributions: P.P.: Conceptualization, Data curation, Methodology, Writing—original draft; G.M.: Conceptualization, Methodology, Formal analysis, Writing—review and editing; T.E.: Methodology, Data curation; T.C.: Formal Analysis, Methodology, Data curation, Writing—review and editing; V.S.: Conceptualization, Investigation, Supervision, Writing—review and editing. All authors have read and agreed to the published version of the manuscript.

Funding: This research received no external funding.

Data Availability Statement: The original contributions presented in the study are included in the article/Supplementary Material, further inquiries can be directed to the corresponding author.

Acknowledgments: The authors would like to acknowledge Robles Hernandez Francisco for his support and guidance throughout the project, Santiago El Awad for assisting with the indentation test, and Kripa Adhikari for assisting with the paper layout and drawings. We also acknowledge the University of Houston Division of Research High Priority Area Research Large Equipment Grant I0503304 for establishing the state-of-the-art 2D-XRD facility used in this study.

Conflicts of Interest: The authors declare that this research was conducted in the absence of any commercial or financial relationships that could be construed as a potential conflict of interest.

References

1. Izadi, M.; Farzaneh, A.; Mohammed, M.; Gibson, I.; Rolfe, B. A review of laser engineered net shaping (LENS) build and process parameters of metallic parts. *Rapid Prototyp. J.* **2020**, *26*, 1059–1078. [CrossRef]
2. Hassen, A.A.; Noakes, M.; Nandwana, P.; Kim, S.; Kunc, V.; Vaidya, U.; Love, L.; Nycz, A. Scaling Up metal additive manufacturing process to fabricate molds for composite manufacturing. *Addit. Manuf.* **2020**, *32*, 101093. [CrossRef]
3. Svetlizky, D.; Zheng, B.; Vyatskikh, A.; Das, M.; Bose, S.; Bandyopadhyay, A.; Schoenung, J.M.; Lavernia, E.J.; Eliaz, N. Laser-based directed energy deposition (DED-LB) of advanced materials. *Mater. Sci. Eng. A* **2022**, *840*, 142967. [CrossRef]
4. Aprilia, A.; Wu, N.; Zhou, W. Repair and restoration of engineering components by laser directed energy deposition. *Mater. Today Proc.* **2022**, *70*, 206–211. [CrossRef]
5. Wang, Y.M.; Voisin, T.; McKeown, J.T.; Ye, J.; Calta, N.P.; Li, Z.; Zeng, Z.; Zhang, Y.; Chen, W.; Roehling, T.T.; et al. Additively manufactured hierarchical stainless steels with high strength and ductility. *Nat. Mater.* **2018**, *17*, 63–70. [CrossRef]
6. Casati, R.; Lemke, J.; Vedani, M. Microstructure and Fracture Behavior of 316L Austenitic Stainless Steel Produced by Selective Laser Melting. *J. Mater. Sci. Technol.* **2016**, *32*, 738–744. [CrossRef]
7. Fedorenko, A.; Fedulov, B.; Kuzminova, Y.; Evlashin, S.; Staroverov, O.; Tretyakov, M.; Lomakin, E.; Akhatov, I. Anisotropy of mechanical properties and residual stress in additively manufactured 316l specimens. *Materials* **2021**, *14*, 7176. [CrossRef]
8. Zhang, B.; Dembinski, L.; Coddet, C. The study of the laser parameters and environment variables effect on mechanical properties of high compact parts elaborated by selective laser melting 316L powder. *Mater. Sci. Eng. A* **2013**, *584*, 21–31. [CrossRef]
9. Heiden, M.J.; Jensen, S.C.; Koepke, J.R.; Saiz, D.J.; Dickens, S.M.; Jared, B.H. Process and feedstock driven microstructure for laser powder bed fusion of 316L stainless steel. *Materialia* **2022**, *21*, 101356. [CrossRef]
10. Wilson, J.M.; Jones, N.; Jin, L.; Shin, Y.C. Laser deposited coatings of Co-Cr-Mo onto Ti-6Al-4V and SS316L substrates for biomedical applications. *J. Biomed. Mater. Res.—Part B Appl. Biomater.* **2013**, *101*, 1124–1132. [CrossRef]
11. Ahn, D.G. Directed Energy Deposition (DED) Process: State of the Art. *Korean Soc. Precis. Eng.* **2021**, *8*, 703–742. [CrossRef]
12. Jensen, S.C.; Koepke, J.R.; Saiz, D.J.; Heiden, M.; Carroll, J.D.; Boyce, B.L.; Jared, B.H. Optimization of Stochastic Feature Properties in Laser Powder Bed Fusion. *Addit. Manuf.* **2022**, *56*, 102943. [CrossRef]
13. King, W.E.; Barth, H.D.; Castillo, V.M.; Gallegos, G.F.; Gibbs, J.W.; Hahn, D.E.; Kamath, C.; Rubenchik, A.M. Observation of keyhole-mode laser melting in laser powder-bed fusion additive manufacturing. *J. Mater. Process. Technol.* **2014**, *214*, 2915–2925. [CrossRef]
14. Roehling, T.T.; Shi, R.; Khairallah, S.A.; Roehling, J.D.; Guss, G.M.; McKeown, J.T.; Matthews, M.J. Controlling grain nucleation and morphology by laser beam shaping in metal additive manufacturing. *Mater. Des.* **2020**, *195*, 109071. [CrossRef]
15. Zheng, B.; Haley, J.C.; Yang, N.; Yee, J.; Terrassa, K.W.; Zhou, Y.; Lavernia, E.J.; Schoenung, J.M. On the evolution of microstructure and defect control in 316L SS components fabricated via directed energy deposition. *Mater. Sci. Eng. A* **2019**, *764*, 138243. [CrossRef]
16. Pathak, P.; Majkic, G.; Selvamanickam, V. Role of customized scan strategies and dwell time on microstructure and properties of additively manufactured 316L stainless steel. *Mater. Sci. Addit. Manuf.* **2024**, *3*, 2676. [CrossRef]
17. Yadollahi, A.; Shamsaei, N.; Thompson, S.M.; Seely, D.W. Effects of process time interval and heat treatment on the mechanical and microstructural properties of direct laser deposited 316L stainless steel. *Mater. Sci. Eng. A* **2015**, *644*, 171–183. [CrossRef]
18. Pacheco, J.T.; Meura, V.H.; Bloemer, P.R.A.; Veiga, M.T.; de Moura Filho, O.C.; Cunha, A.; Teixeira, M.F. Laser directed energy deposition of AISI 316L stainless steel: The effect of build direction on mechanical properties in as-built and heat-treated conditions. *Adv. Ind. Manuf. Eng.* **2022**, *4*, 100079. [CrossRef]
19. Ribeiro, K.S.B.; Mariani, F.E.; Coelho, R.T. A Study of Different Deposition Strategies in Direct Energy Deposition (DED) Processes. *Procedia Manuf.* **2020**, *48*, 663–670. [CrossRef]
20. Lin, P.Y.; Shen, F.C.; Wu, K.T.; Hwang, S.J.; Lee, H.H. Process optimization for directed energy deposition of SS316L components. *Int. J. Adv. Manuf. Technol.* **2020**, *111*, 1387–1400. [CrossRef]
21. Balhara, H.; Botcha, B.; Wolff, S.; Bukkapatnam, S. Ripple formation and its effect on the multi-scale microstructure of Directed Energy Deposition (DED)-printed 316L components. *arXiv* **2021**, arXiv:2111.11601.
22. Zheng, B.; Zhou, Y.; Smugeresky, J.E.; Schoenung, J.M.; Lavernia, E.J. Thermal behavior and microstructural evolution during laser deposition with laser-engineered net shaping: Part I. Numerical calculations. *Metall. Mater. Trans. A Phys. Metall. Mater. Sci.* **2008**, *39*, 2228–2236. [CrossRef]
23. Pathak, P.; Dzhurinskiy, D.; Elkin, A.; Shornikov, P.; Dautov, S.; Ivanov, V. Enhanced High-Temperature YSZ-polyester Abradable Honeycomb Seal Structures. *J. Therm. Spray Technol.* **2022**, *31*, 307–314. [CrossRef] [PubMed]
24. Manvatkar, V.D.; Gokhale, A.A.; Reddy, G.J.; Venkataramana, A.; De, A. Estimation of melt pool dimensions, thermal cycle, and hardness distribution in the laser-engineered net shaping process of austenitic stainless steel. *Metall. Mater. Trans. A Phys. Metall. Mater. Sci.* **2011**, *42*, 4080–4087. [CrossRef]
25. Mukherjee, T.; Zuback, J.S.; De, A.; DebRoy, T. Printability of alloys for additive manufacturing. *Sci. Rep.* **2016**, *6*, 19717. [CrossRef] [PubMed]

26. Mohr, G.; Altenburg, S.J.; Hilgenberg, K. Effects of inter layer time and build height on resulting properties of 316L stainless steel processed by laser powder bed fusion. *Addit. Manuf.* **2020**, *32*, 101080. [CrossRef]
27. Salman, O.O.; Gammer, C.; Chaubey, A.K.; Eckert, J.; Scudino, S. Effect of heat treatment on microstructure and mechanical properties of 316L steel synthesized by selective laser melting. *Mater. Sci. Eng. A* **2019**, *748*, 205–212. [CrossRef]
28. Carminati, M.; Quarto, M.; D'Urso, G.; Giardini, C.; Maccarini, G. Mechanical Characterization of AISI 316L Samples Printed Using Material Extrusion. *Appl. Sci.* **2022**, *12*, 1433. [CrossRef]
29. Kuzminova, Y.O.; Firsov, D.G.; Konev, S.D.; Dudin, A.A.; Dagesyan, S.A.; Akhatov, I.S.; Evlashin, S.A. Structure control of 316L stainless steel through an additive manufacturing. *Lett. Mater.* **2019**, *9*, 551–555. [CrossRef]
30. Chadha, K.; Tian, Y.; Spray, J.G.; Aranas, C. Effect of annealing heat treatment on the microstructural evolution and mechanical properties of hot isostatic pressed 316L stainless steel fabricated by laser powder bed fusion. *Metals* **2020**, *10*, 753. [CrossRef]
31. Mirzababaei, S.; Paul, B.K.; Pasebani, S. Microstructure-property relationship in binder jet produced and vacuum sintered 316 L. *Addit. Manuf.* **2022**, *53*, 102720. [CrossRef]
32. Zhang, G.; Lu, X.; Li, J.; Chen, J.; Lin, X.; Wang, M.; Tan, H.; Huang, W. In-situ grain structure control in directed energy deposition of Ti6Al4V. *Addit. Manuf.* **2022**, *55*, 102865. [CrossRef]
33. Heigel, J.C.; Michaleris, P.; Reutzel, E.W. Thermo-mechanical model development and validation of directed energy deposition additive manufacturing of Ti-6Al-4V. *Addit. Manuf.* **2015**, *5*, 9–19. [CrossRef]
34. Sciammarella, F.M.; Najafabadi, B.S. Processing parameter doe for 316l using directed energy deposition. *J. Manuf. Mater. Process.* **2018**, *2*, 61. [CrossRef]
35. Gong, H.; Nadimpalli, V.K.; Rafi, K.; Starr, T.; Stucker, B. Micro-CT Evaluation of Defects in Ti-6Al-4V Parts Fabricated by Metal Additive Manufacturing. *Technologies* **2019**, *7*, 44. [CrossRef]
36. Ziętala, M.; Durejko, T.; Polański, M.; Kunce, I.; Płociński, T.; Zieliński, W.; Łazińska, M.; Stępniowski, W.; Czujko, T.; Kurzydłowski, K.J.; et al. The microstructure, mechanical properties and corrosion resistance of 316 L stainless steel fabricated using laser engineered net shaping. *Mater. Sci. Eng. A* **2016**, *677*, 1–10. [CrossRef]
37. Kruth, J.P.; Bartscher, M.; Carmignato, S.; Schmitt, R.; De Chiffre, L.; Weckenmann, A. Computed tomography for dimensional metrology. *CIRP Ann.—Manuf. Technol.* **2011**, *60*, 821–842. [CrossRef]
38. Smith, K.L.; Ortega, K.B. Use of a Two-Dimensional, Position Sensitive Detector for Collecting Pole Figures. *Adv. X-Ray Anal.* **1992**, *36*, 641–647. [CrossRef]
39. He, B.B. Introduction to two-dimensional X-Ray diffraction. *Powder Diffr.* **2003**, *18*, 71–85. [CrossRef]
40. Cho, J.Y.; Xu, W.; Brandt, M.; Qian, M. Selective laser melting-fabricated Ti-6Al-4V alloy: Microstructural inhomogeneity, consequent variations in elastic modulus and implications. *Opt. Laser Technol.* **2019**, *111*, 664–670. [CrossRef]
41. He, B.B.; Preckwinkel, U.; Smith, K.L. Stress and texture analysis with two-dimensional X-Ray diffraction. *Mater. Sci. Forum* **2002**, *404–407*, 109–114. [CrossRef]
42. Thompson, A.; Maskery, I.; Leach, R.K. X-Ray computed tomography for additive manufacturing: A review. *Meas. Sci. Technol.* **2016**, *27*, 072001. [CrossRef]
43. Lopez, E.; Felgueiras, T.; Grunert, C.; Brückner, F.; Riede, M.; Seidel, A.; Marquardt, A.; Leyens, C.; Beyer, E. Evaluation of 3D-printed parts by means of high-performance computer tomography. *J. Laser Appl.* **2018**, *30*, 032307. [CrossRef]
44. Carlton, H.D.; Haboub, A.; Gallegos, G.F.; Parkinson, D.Y.; Macdowell, A.A. Materials Science & Engineering A Damage evolution and failure mechanisms in additively manufactured stainless steel. *Mater. Sci. Eng. A* **2016**, *651*, 406–414. [CrossRef]
45. Mazumder, J.; Schifferer, A.; Choi, J. Direct materials deposition: Designed macro and microstructure. *Mater. Res. Innov.* **1999**, *3*, 118–131. [CrossRef]
46. Bjerregaard, L.; Geels, K.; Ottesen, B.; Rückert, M. Metalog Guide. 2020. Available online: https://www.struers.com/en/Library#brochures (accessed on 2 January 2022).
47. Dzhurinskiy, D.; Babu, A.; Pathak, P.; Elkin, A.; Dautov, S.; Shornikov, P. Microstructure and wear properties of atmospheric plasma-sprayed Cr3C2-NiCr composite coatings. *Surf. Coat. Technol.* **2021**, *428*, 127904. [CrossRef]
48. El Awad, S.; Stefaniuk, D.; Krakowiak, K.J. Determination of elastic and flexural strength properties of multi-scale materials via indentation assisted micro-bending experiment and inverse analysis. *Mech. Mater.* **2021**, *158*, 103889. [CrossRef]
49. Joshi, B.; Li, X.; Oz, Y.; Wang, J.; Shan, X.; Mo, Y.L. Effects of fiber dosage, loading orientation and stress on frequency response of enhanced Carbon Nano-Fiber Aggregates. *Compos. Part B Eng.* **2021**, *225*, 109257. [CrossRef]
50. *ASTM F3637-23*; Standard Guide for Additive Manufacturing of Metal—Finished Part Properties—Methods for Relative Density Measurement. ASTM: West Conshohocken, PA, USA, 2023.
51. Puichaud, A.-H.; Flament, C.; Chniouel, A.; Lomello, F.; Rouesne, E.; Giroux, P.-F.; Maskrot, H.; Schuster, F.; Béchade, J.-L. Microstructure and mechanical properties relationship of additively manufactured 316L stainless steel by selective laser melting. *EPJ Nucl. Sci. Technol.* **2019**, *5*, 23. [CrossRef]
52. Rupert, A.N.; McCausland, P.J.A.; Flemming, R.L. Ordinary chondrite shock stage quantification using in situ 2-D X-Ray diffraction of olivine. *Meteorit. Planet. Sci.* **2020**, *55*, 2224–2240. [CrossRef]
53. Kim, F.H.; Moylan, S.P. Literature Review of Metal Additive Manufacturing Defects. *NIST Adv. Manuf. Ser.* **2018**, 1–17. Available online: http://nvlpubs.nist.gov/nistpubs/ams/NIST.AMS.100-16.pdf (accessed on 1 June 2021).
54. Panov, D.; Oreshkin, O.; Voloskov, B.; Petrovskiy, V.; Shishkovsky, I. Pore healing effect of laser polishing and its influence on fatigue properties of SLM manufactured SS316L parts. *Opt. Laser Technol.* **2022**, *156*, 108535. [CrossRef]

55. Terrassa, K.L.; Haley, J.C.; MacDonald, B.E.; Schoenung, J.M. Reuse of powder feedstock for directed energy deposition. *Powder Technol.* **2018**, *338*, 819–829. [CrossRef]
56. Susan, D.F.; Puskar, J.D.; Brooks, J.A.; Robino, C.V. Quantitative characterization of porosity in stainless steel LENS powders and deposits. *Mater. Charact.* **2006**, *57*, 36–43. [CrossRef]
57. Courtois, M.; Carin, M.; Le Masson, P.; Gaied, S. A two-dimensional axially-symmetric model of keyhole and melt pool dynamics during spot laser welding. *Metall. Res. Technol.* **2013**, *110*, 165–173. [CrossRef]
58. Wits, W.W.; Scolaro, E.; Amsterdam, E.; Clare, A.T. The role of scan strategies in fatigue performance for laser powder bed fusion. *CIRP Ann.* **2022**, *71*, 185–188. [CrossRef]
59. Plessis, A.D.; Razavi, S.M.J.; Wan, D.; Berto, F.; Imdaadulah, A.; Beamer, C.; Shipley, J.; MacDonald, E. Fatigue performance of shelled additively manufactured parts subjected to hot isostatic pressing. *Addit. Manuf.* **2022**, *51*, 102607. [CrossRef]
60. Foteinopoulos, P.; Papacharalampopoulos, A.; Angelopoulos, K.; Stavropoulos, P. Development of a simulation approach for laser powder bed fusion based on scanning strategy selection. *Int. J. Adv. Manuf. Technol.* **2020**, *108*, 3085–3100. [CrossRef]

Disclaimer/Publisher's Note: The statements, opinions and data contained in all publications are solely those of the individual author(s) and contributor(s) and not of MDPI and/or the editor(s). MDPI and/or the editor(s) disclaim responsibility for any injury to people or property resulting from any ideas, methods, instructions or products referred to in the content.